



HAL
open science

Investigation of lasing in highly strained germanium at the crossover to direct band gap

F. Armand Pilon, Y-M. Niquet, J. Chretien, N. Pauc, V. Reboud, V. Calvo, J. Widiez, J. Hartmann, A. Chelnokov, J. Faist, et al.

► **To cite this version:**

F. Armand Pilon, Y-M. Niquet, J. Chretien, N. Pauc, V. Reboud, et al.. Investigation of lasing in highly strained germanium at the crossover to direct band gap. *Physical Review Research*, 2022, 4 (3), pp.033050. 10.1103/PhysRevResearch.4.033050 . hal-04014816

HAL Id: hal-04014816

<https://hal.science/hal-04014816v1>

Submitted on 25 Sep 2024





HAL is a multi-disciplinary open access archive for the deposit and dissemination of scientific research documents, whether they are published or not. The documents may come from teaching and research institutions in France or abroad, or from public or private research centers.

L'archive ouverte pluridisciplinaire **HAL**, est destinée au dépôt et à la diffusion de documents scientifiques de niveau recherche, publiés ou non, émanant des établissements d'enseignement et de recherche français ou étrangers, des laboratoires publics ou privés.



Distributed under a Creative Commons Attribution 4.0 International License

Investigation of lasing in highly strained germanium at the crossover to direct band gap

F. T. Armand Pilon ^{1,5,*} Y-M. Niquet ² J. Chretien,³ N. Pauc,³ V. Reboud,⁴ V. Calvo,³ J. Widiez ⁴ J. M. Hartmann,⁴ A. Chelnokov,⁴ J. Faist,⁵ and H. Sigg ^{1,†}

¹Laboratory for X-ray Nanoscience & Technologies, Paul Scherrer Institut, 5232 Villigen, Switzerland

²Université Grenoble Alpes, CEA, IRIG, MEM, 38000 Grenoble, France

³Université Grenoble Alpes, CEA, Grenoble INP, IRIG, PHELIQS, 38000 Grenoble, France

⁴Université Grenoble Alpes, CEA, LETI, 38054 Grenoble, France

⁵Institute for Quantum Electronics, ETH Zürich, 8093 Zürich, Switzerland



(Received 31 January 2022; revised 31 May 2022; accepted 9 June 2022; published 18 July 2022)

Efficient and cost-effective Si-compatible lasers are a longstanding wish of the optoelectronic industry. In principle, there are two options. For many applications, lasers based on III-V compounds provide compelling solutions, even if the integration is complex and therefore costly. However, where low costs and also high integration density are crucial, group-IV-based lasers—made of Ge and GeSn, for example—could be an alternative, provided their performance can be improved. Such progress will come with better materials but also with the development of a more profound understanding of their optical properties. In this work, we demonstrate, using Ge microbridges with strain up to 6.6%, a powerful method for determining the population inversion gain and the material and optical losses of group IV lasers. This is done by deriving the values for the injection carrier densities and the cavity losses from the measurement of the change of the refractive index and the mode linewidth, respectively. We observe a laser threshold consistent with optical gain. Material loss values are obtained from a tight-binding calculation. Lasing in Ge—at steady-state—is found to be limited to low temperatures in a narrow regime of tensile strain at the crossover to the direct-band-gap band structure. We explain this observation by parasitic inter-valence-band absorption that increases rapidly with higher injection densities and temperature. *N*-doping seems to reduce the material loss at low excitation, but it does not extend the lasing regime. We also discuss the impact of the optically inactive carriers in the L-valley on the linewidth of group IV lasers.

DOI: [10.1103/PhysRevResearch.4.033050](https://doi.org/10.1103/PhysRevResearch.4.033050)

I. INTRODUCTION

Today, germanium-based materials, strained [1] or alloyed with Sn [2,3], form the most advanced platform for group-IV lasing. However, despite encouraging results [4–15], all group-IV lasing performances are behind those of group III-V based lasers integrated on silicon using direct growth on prepatterned [16] or planar layers of quantum dots [17,18], quantum wells [19] or quantum-cascade structures [20]. There is definitely the possibility to close this gap by improving the materials and strengthening the knowledge of the fundamental mechanisms relevant for lasing in group IV. For the latter, we miss a coherent description of the dependence of lasing performances on the band offset and doping. It is also essential to understand the role of parasitic losses, such as the inter-valence-band (IVB) absorption [21] and its dependence on the carrier injection and temperature. Moreover, even essential details of the band structure, such as the band offset between

the band edges at Γ and L and its dependence on the strain, are not fully settled yet, neither for Ge [22] nor for GeSn [23] alloys. To improve the performance of group IV lasers, this would have to be known precisely.

Here, we address these points for the strained Ge system, where we can benefit from thoroughly developed tools to calculate band structure [24] and properties relevant for transport [25] and lasing [26,27]. Moreover, Ge is attractive not only for laser benchmarking, but also because of its recent use in quantum technology as a spin qubit [28–30]. The possibility to fabricate from the same material quantum gates as well as a laser source provides further motivation for this study.

The bottleneck that must be overcome to achieve lasing action with pristine Ge is the low population of carriers at the center of the Brillouin zone (Γ), where optical transitions are allowed. Being an indirect semiconductor, Ge differs from standard direct-band-gap semiconductors such as GaAs, where basically only such Γ states are occupied. There are two approaches to enhance the carrier population at Γ in Ge: (i) The initial proposal suggested to use strong *n*-doping with phosphorus [31]. However, the related experiments showed contradictory results. Whereas the photoluminescence [32] and electroluminescence [33,34] from optical cavities made of such highly doped Ge had been attributed to lasing, the absorption studied under optical pumping on similar material in Refs. [35,36] did not reveal the net gain required for lasing. Alternatively, by applying tensile strain, (ii) we can control

*francesco.tap@gmail.com

†hans.sigg@psi.ch

Published by the American Physical Society under the terms of the [Creative Commons Attribution 4.0 International license](https://creativecommons.org/licenses/by/4.0/). Further distribution of this work must maintain attribution to the author(s) and the published article's title, journal citation, and DOI.

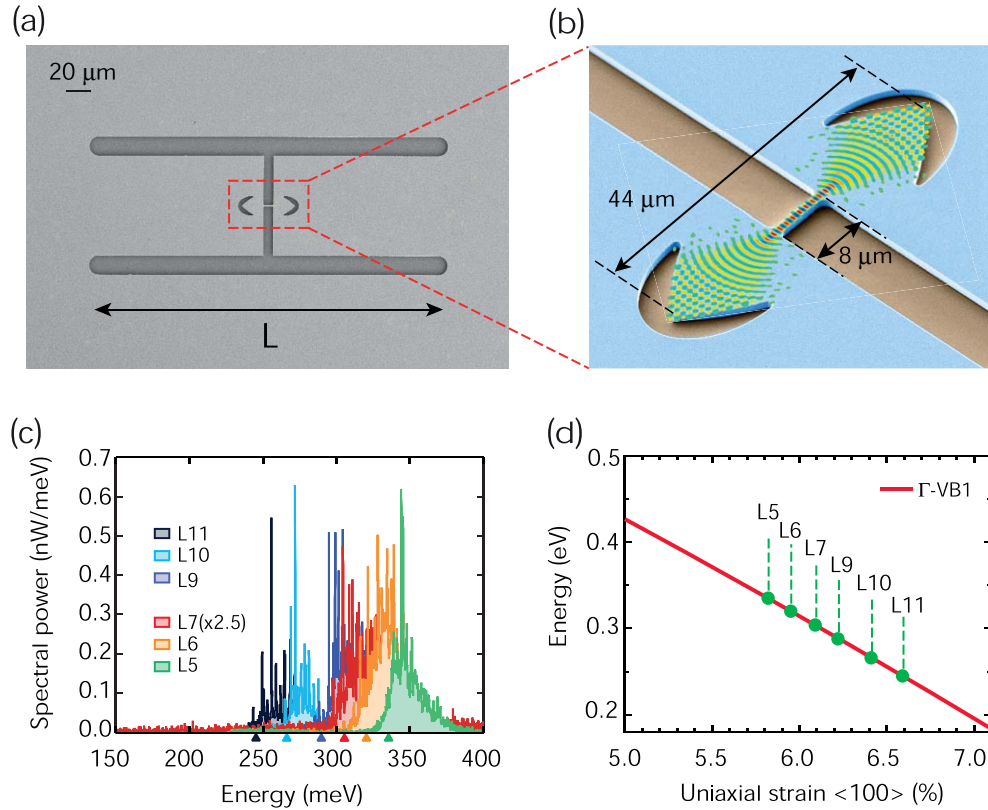


FIG. 1. (a) Top-view scanning electron microscope (SEM) image of a strained germanium microbridge with a total length of L . (b) Tilted SEM image in false color of a corner cube cavity. Superimposed, the finite-element method (FEM) simulation of the out-of-plane electric field of the fundamental TE cavity mode. (c) Samples L5–L11 photoluminescence at 15 K upon continuous-wave excitation of about 6 mW. The band gap, as inferred from the PL background, is indicated by the triangles on the x -axis. (d) Tight-binding Γ band-edge dependence on strain (red line) together with the experimental band gap (in green). The extracted strain values are given in Table I.

the population at the Γ -point by gradually closing the offset between the band edge at the Γ - and L-points until we have reached and even passed the crossover to the direct band gap, where—in a situation similar to that of GaAs—the lowest energy states in Γ are below those of L. Then, population inversion between the relevant states and thus lasing become possible.

To systematically investigate this transition regime from an indirect to a direct semiconductor, we make use of the recently developed strain amplification approach [37,38]. It enables us to study the evolution of lasing—using the same doped or undoped base material—as a function of just the strain. Lasing under tensile strain has also been investigated for the GeSn system [9,12], however its dependence on the strain has not been systematically studied.

The organization of the paper follows our experimental approach: we first describe the strain amplification concept [37,38] used to produce a series of high-quality optical cavities with strain up to 4.2% at room temperature, reaching up to 6.6% at low temperature. For all samples, the low-temperature photoluminescence spectra of the cavity modes are investigated in dependence on the excitation power, i.e., the carrier density. The latter was determined from the plasma shift of the dielectric function. We infer the strain from matching the experimental band gap to the calculated band structure obtained using the tight-binding (TB) approach [24]. With the same model, we compute the matrix elements needed for

the interband gain and the intra-valence-band material loss calculation. We show that by choosing appropriate values for the carrier temperature and line broadening, as well as the cavity losses, the TB-model accurately predicts lasing thresholds for samples with approximately 6% of strain for excitation around $2 \times 10^{18} \text{ cm}^{-3}$. The model also explains the observed lasing rollover at higher excitations and when the cryostat temperature exceeds 30 K. Via the analysis of the cavity modes' linewidth—similarly to the work of Petykiewicz *et al.* [39]—we deduce the cavity quality factor and we gather an overall understanding of the gain and loss mechanism in our tensile strained Ge cavities. We then pin down the crossover to a direct band gap for uniaxially strained Ge at 6.1%. In the final experimental sections, we study the mode linewidth of moderately n -type doped material with high strain, and we discuss a peculiar deviation of the usual Schawlow-Townes laser linewidth theory [40] for the case of only modestly direct-band-gap group IV lasers.

II. SAMPLES

In this experiment, we study the optical properties at low temperatures of highly strained Ge microbridges that are suspended and embedded into an optical cavity. The high strain is achieved by patterning along $\langle 100 \rangle$ and selectively underetching a GeOI layer with a builtin biaxial tensile strain ε_0 of 0.16%. The layers were undoped or doped *in situ* by

phosphorus. The strain amplification method has been explained in detail in [37,1,41]. We employed samples with notations L5, L6, L7 on chip A and L9, L10, L11 on chip B obtained from two consecutive processing runs. The labels indicate structures with progressively increasing total pad length L (c.f. Fig. 1(a)) in the range of $280\ \mu\text{m}$ to $400\ \mu\text{m}$. The length L determines the uniaxial tensile strain, which ranges from 3.7 up to 4.2% at room temperature (RT) as measured via Raman scattering. The strained microbridge of length $l_b = 8\ \mu\text{m}$ is integrated in a strain-maintaining optical cavity with two corner cube reflectors, at a distance $l_c = 44\ \mu\text{m}$. The cavity is shown in Fig. 1(b), together with the optical mode pattern as calculated with *Comsol Multi Physics*.

The microbridge structures are mounted in a cryostat with a base temperature of 15 K, and they are excited with a diode laser running in continuous wave with an energy of $h\nu_{\text{ext}} = 590\ \text{meV}$ ($\lambda = 2.15\ \mu\text{m}$) and an excitation diameter (i.e., a full width at half-maximum) of about $8.7\ \mu\text{m}$. The photon energy of the excitation is well below the band gap of unstrained Ge to guarantee low loss in the pad region, which is essentially unstrained. Throughout this paper, the reported excitation power is defined as the total power at the sample position. Due to the excellent thermal conductivity of Ge at low temperature (1.7 kW/mK at 15 K), the temperature increase of the samples is less than 10 K at the excitation of 10 mW, even when considering a possible reduction of the thermal conductivity by one order of magnitude due to the structure's finite size. The optical spectra are recorded via a Fourier transform infrared spectrometer (Bruker Vertex 70) running in the fast scanning mode with an instrumental resolution of $0.5\ \text{cm}^{-1}$, corresponding to $62\ \mu\text{eV}$.

The low-temperature photoluminescence (PL) spectra of samples L5–L11 are reported in Fig. 1(c). Each of the samples shows a broad spontaneous emission strongly modulated by Fabry-Pérot cavity modes. The higher the strain of the sample, the lower is the PL energy. Compared to RT—cf. Appendix A—the PL onset is redshifted, in line with a tensile strain increase when cooling the samples [41]. We converted the measured PL signal to the spectral power of light collected by the microscope using the calibration procedure described in [1]. This procedure could not be applied for L7 because of a misaligned detector. Its spectral power was adjusted by an arbitrary factor of 2.5 for better visibility in Fig. 1(c). Figure 1(d) reports the Γ -VB1 band-gap energy dependence on strain at low temperature as obtained from the tight-binding (TB) simulations [24,1]. As per Fig. 1(d), we deduce the strain of the samples from the position of the band gap. This approach was verified previously by Guillois *et al.* [22] via electromodulation spectroscopy on similar microbridges with strain up to 3.3% calibrated by x-ray microdiffraction [42]. Here, we relate the band gap to the photon energy at the half-maximum spectral intensity of the photoluminescence background; cf. the x -axis of Fig. 1(c). This simple method is particularly well suited in the case of strong cavity modes. Corresponding strain values are summarized in Table I.

From the correlation of the PL spectra with Raman measurements taken at room temperature, cf. Appendix A, we obtain that the thus defined band-gap values fit nicely the strain dependence of the TB model up to 4.2%.

TABLE I. Band-gap energy extracted from the photoluminescence at 15 K and the deduced strain value [cf. Figs. 1(b) and 1(c)].

	L5	L6	L7/L7*	L9	L10	L11
Band gap (meV)	335	320	304	288	266	245
Strain (%)	5.82	5.95	6.09	6.22	6.41	6.59

III. CAVITY SPECTRA AND LASING THRESHOLD

Figures 2(a)–2(e) show a series of power-dependent cavity-PL spectra taken at 15 K for samples L5, L6, and L7*, L9, L10, and L11. The sample denoted as L7* belongs to chip B. It has the geometry of L9 but the PL spectra characteristics and onset of the L7 cavities of chip A; cf. Appendix B. We may thus safely assume that the strain of that particular sample L9, henceforth referred to as L7*, is the same as for L7. To enable measurements under identical conditions on a series of differently strained samples, we use in the following the results of L7* together with L9, L10, and L11.

Samples are excited up to 15 mW, corresponding to a carrier density of about $3.7 \times 10^{18}\ \text{cm}^{-3}$. This conversion is based on the observed frequency shift of the cavity modes induced by the electron-hole plasma dispersion effect, as shown in Appendix C. The factor of $0.25 \times 10^{18}\ \text{cm}^{-3}/\text{mW}$ is found to be valid for all samples. This value corresponds roughly to a case with an absorbed fraction and a recombination time of 40% and 5 ns, respectively. The latter is in agreement with the surface recombination time found in a previous pump probe study of the $2\text{-}\mu\text{m}$ -thick GeOI source material used here [43], while the 40% is a fair estimate for strained Ge when considering the cavity effect created by multiple reflections within the bridge and via the Si substrate.

The spectra shown in Fig. 2 can be grouped in three strain ranges. For the lowest strains, Figs. 2(a) and 2(b), the spectra show a broad photoluminescence background modulated by Fabry-Pérot cavity modes. For intermediate strains, the spectral emissions of L7* and L9 in Figs. 2(c) and 2(d) show a similar combination of background and multimode emission, but only up to about 6 mW excitation. Above about 9 mW, there is a single-mode peak in the PL spectra of L7* and L9: its spectral peak intensity sharply increases by about two to three orders of magnitude above the spontaneous emission background. Remarkably, for the highest strains, Figs. 2(e) and 2(f), the spectra of L10 and L11 are again multimode up to the highest excitation power.

The emission obtained for the samples with intermediate strains not only exhibits a single mode, but it also reveals a steep increase of the total emitted power, as shown in Fig. 3(a), clearly demonstrating lasing action in L7* and L9. Conversely, L5 and L6 as well as L10 and L11, the samples with the lowest and the highest strains, do not lase, as neither single-mode operation nor a noticeable increase of emission efficiency is observed.

From the intersection between the linearly extrapolated PL emission at high and low excitation power shown in Fig. 3(a), threshold powers of 9.6 and 8.6 mW for, respectively, L7*—as well as L7 shown in Appendix B—and L9 are obtained. These values, using the above-mentioned conversion factor, correspond to a carrier density $N_{th} = 2.4(2.1) \times 10^{18}\ \text{cm}^{-3}$ for

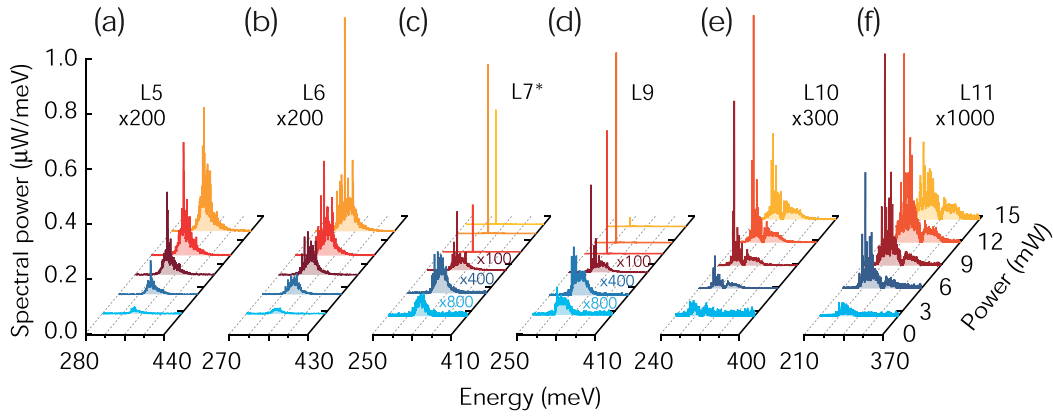


FIG. 2. PL emission power collected at the exit of the microscope vs continuous-wave excitation power taken at 15 K of (a) L5, (b) L6, (c) L7*, (d) L9, (e) L10, and (f) L11 microbridge cavities. Above threshold, the L7* and L9 spectral emissions of (c) and (d) are dominated by a single mode at 311 and 295 meV, respectively.

L7* (L9). For both samples, the linear increase in the emitted intensity is followed by a striking rollover. For L9, the rollover point occurs at an excitation power lower than for L7*.

In Fig. 3(b), we show the light-in light-out curves of lasing sample L9 as a function of temperature in linear scale. The temperature is increased in steps of 5 K from 15 up to 35 K. By raising the temperature, the lasing efficiency rapidly degrades until at 35 K the lasing is suppressed. This behavior, together with the rollover at higher excitation as well as the threshold values of L7* and L9 near $2 \times 10^{18} \text{ cm}^{-3}$, conforms to the predictions detailed in the following.

IV. BAND STRUCTURE, GAIN, AND LOSS

Figure 4(a) represents the band structure of germanium under a uniaxially loaded tensile strain of 6% (shown in orange) when ΔE , the offset between the Γ and the L band edges, is practically zero. The blue lines represent the band structure for relaxed Ge when the strain is zero and ΔE is about 140 meV. Details of the used tight-binding model are given in Ref. [24]. The strongest optical transitions are indicated by the green and red arrows representing, respectively, the interband transitions providing gain and the intervalence band (IVB) transitions responsible for the main material loss, α_m . Figure 4(b) shows

gain spectra for the barely direct-band-gap case with $\Delta E = -3 \text{ meV}$ and carrier density up to $5 \times 10^{18} \text{ cm}^{-3}$. We give further details about the optical gain model in Appendix D.

Carrier temperature and state broadening for this calculation are set to 30 K and 10 meV, respectively. The latter comes from a previous IVB absorption study of doped Ge [44] at low temperature. As no corresponding study was made for the interband excitation, its state broadening is assumed to be the same for simplicity. The carrier temperature is expected to be higher than the base temperature set for the cryostat and possibly also above that of the phonon bath, because carriers can be heated by the injection and might be out of equilibrium, albeit only weakly. However, as a change of the base temperature by only 20 K—as demonstrated in Fig. 3(b)—is able to switch off the lasing, we know that the heating of the carriers by injection is low and will not exceed 30 K at the 15 K base temperature, as we will conclude later.

The open circles shown in Fig. 4(b) mark the peak gain for a selection of excitation densities. While the peak gain is shifting to higher energies with increasing excitation, a transparency band with zero absorption develops at the high-energy side of the spectra. This behavior is typical for marginally direct systems; it can be attributed to the filling of the lowest valence-band states near Γ by a large num-

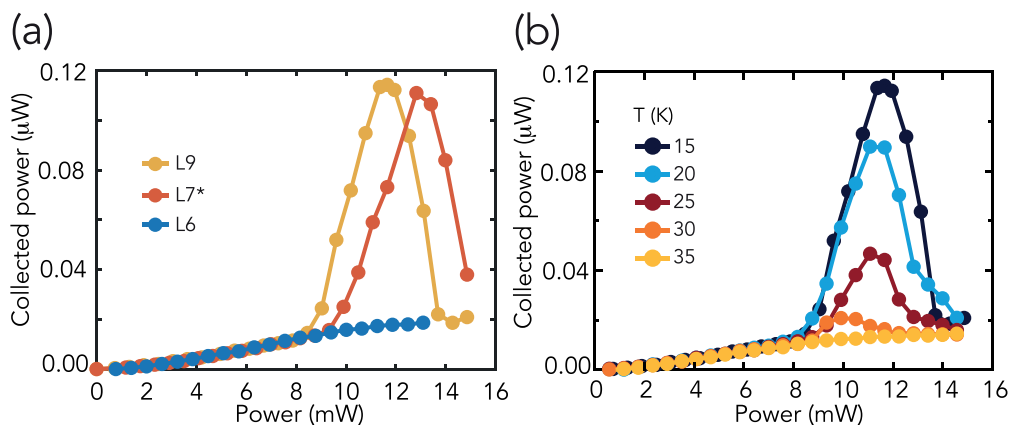


FIG. 3. (a) PL power at the exit of the microscope as a function of the excitation power for samples L6, L7*, and L9 at 15 K. (b) Collected power of sample L9 for different temperatures, from 15 up to 35 K.

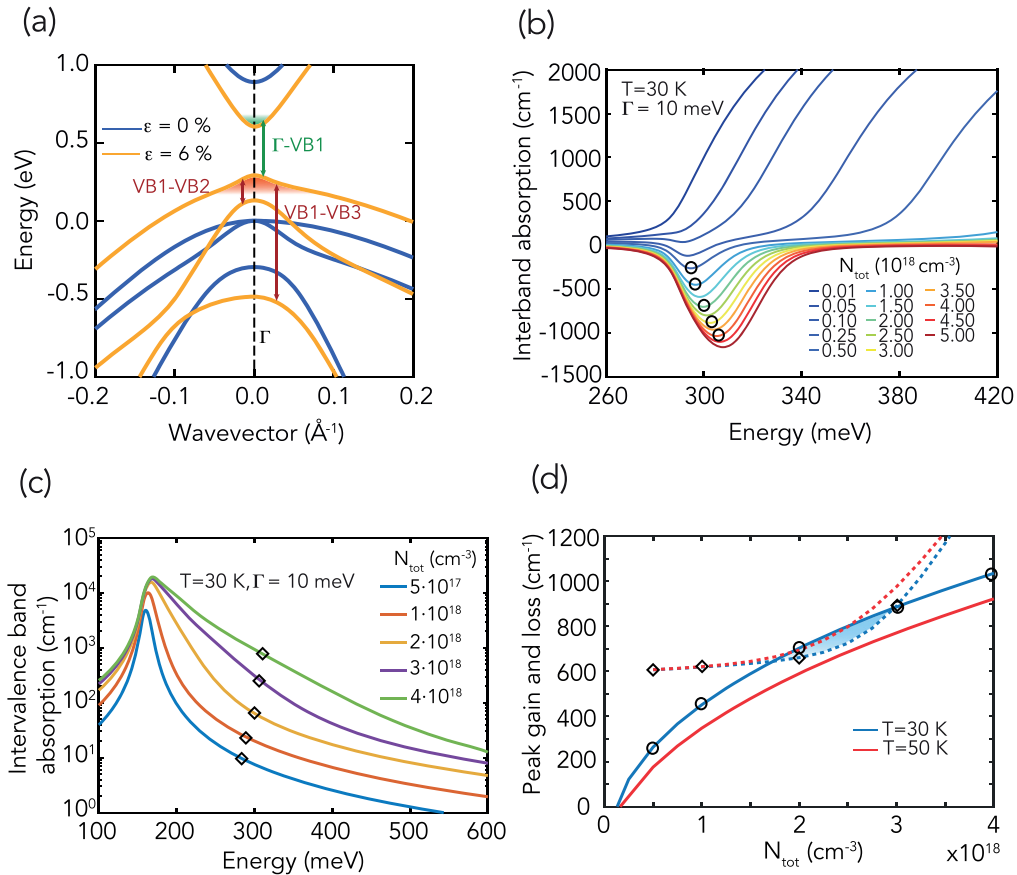


FIG. 4. Modeling of Ge's band structure, gain and loss. (a) Band structure of germanium near the Γ point, calculated with the tight-binding model for strain along the [001] direction of 6% (orange) when $\Delta E = 0$, and for 0% (blue) when $\Delta E = 140\text{ meV}$. The green and red arrows indicate the interband and intervalence band transitions. (b) Interband absorption spectra for carrier excitation up to $5 \times 10^{18}\text{ cm}^{-3}$ for $\Delta E = -3\text{ meV}$, with a band gap about 290 meV . A transparency region develops above the gain region. (c) Intervalence band absorption spectra for 6% of strain and excitation densities of $0.5, 1, 2, 3,$ and $4 \times 10^{18}\text{ cm}^{-3}$. In (b) and (c) the electron temperature and state broadening are assumed to be 30 K and 10 meV , respectively. (d) Peak optical gain (solid lines) as a function of the injection density for an offset $\Delta E = -3\text{ meV}$, extracted from (b) (cf. black circles). The total loss (dashed lines) as a function of the carrier density is obtained by adding the intervalence band absorption calculated at peak gain energy [cf. the open square in (c)] on top of the optical loss of 600 cm^{-1} . The latter value is obtained from the experiment and is normalized to the mode filling of 0.17 ; see the main text. The blue and red represent the carrier temperatures of 30 and 50 K , respectively. For 30 K , the lasing threshold is found to be near $2 \times 10^{18}\text{ cm}^{-3}$ while at higher densities ($> 2.5 \times 10^{18}\text{ cm}^{-3}$) a laser roll-over occurs because of the steeply rising IVB absorption. When the carrier temperature is set at 50 K , the gain (red solid line) does not overcome the loss (red dashed line).

ber of holes, while most of the excited electrons are in the L-conduction band. Figure 4(c) shows the IVB loss spectra (α_m) for several excitation densities assuming the same carrier temperature and state broadening. Curves are tagged by open squares at the photon energy corresponding to the peak gain at the same carrier density. The IVB absorption strongly increases for decreasing energies, and its high-energy tail is characterized by a rapid increase for carrier densities and temperatures above $2 \times 10^{18}\text{ cm}^{-3}$ and 30 K , respectively. Details of our IVB absorption model are presented in Appendix E together with an analysis of its dependence on temperature and state broadening. The rapid increase of the IVB absorption is due to holes filling the states farther apart from the Γ point in reciprocal space; cf. Fig. 4(a). The strongest contribution comes from the transitions between VB1 and VB2, as indicated by the red arrow in Fig. 4(a). The transitions from VB1 to the split-off (VB3) occur at energies

larger than 650 meV and thus are not relevant in the present case.

Figure 4(d) shows the dependence on the excitation density of the peak gain (blue curve) and the corresponding loss (blue dashed curve) at 30 K . Lasing is expected when the modal gain overcomes the total loss, which includes material and optical or cavity loss, α_c . The latter is experimentally found to be 103 cm^{-1} , as detailed in the next section. The material loss can be extracted from Fig. 4(c). It has to be evaluated at the emission energy where the gain is maximal, as indicated by the open squares. We show in Fig. 4(d) the case of a marginally direct band structure, with an offset $\Delta E = -3\text{ meV}$. In this case, the gain overcomes the total loss at an injection density of about $2 \times 10^{18}\text{ cm}^{-3}$. For zero offset (not shown), the gain does not overcome the IVB loss anymore, demonstrating that the offset ΔE is the main parameter driving the gain at the low temperatures probed here. Optical broadening and effective carrier temperature also have some impact on gain and loss,

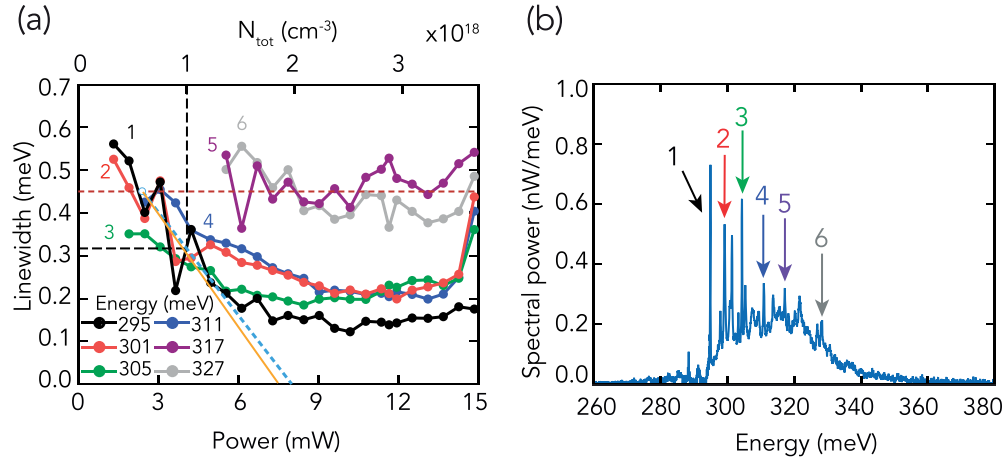


FIG. 5. (a) L9 linewidth at 15 K as a function of the excitation power of the modes labeled in (b). The horizontal dashed line at 0.45 meV indicates transparency. The differential net gain is extracted from the linear regression between the transparency point and the power corresponding to $N_r = 10^{18} \text{ cm}^{-3}$. It is shown as a dashed light blue line. The orange line starting as well from transparency is obtained from the model of Figs. 4(b) and 4(c). (b) L9 spectral emission at 15 K for an excitation power $P = 6.12 \text{ mW}$.

but only marginally. We observe that, for any combination of optical broadening and effective temperature variation in the range of $\pm 5 \text{ meV}$ and $\pm 15 \text{ K}$, respectively, the offset at which the gain may overcome the loss shifts by less than $\pm 2 \text{ meV}$. However, we reach the best overall agreement with the experiments with the above values of broadening and temperature.

Due to the fast-growing IVB absorption with density and temperature, lasing is achieved neither at higher excitation nor at elevated temperature. As shown in Fig. 4(d), the low temperature loss curve (blue dashed line) overcomes the gain at around $3 \times 10^{18} \text{ cm}^{-3}$. At 50 K, the gain (red solid line) does not prevail over the loss (red dashed line). Both predictions are in good agreement with the experiments presented in Figs. 3(a) and 3(b).

In fact, by considering in our gain calculation the offset ΔE as a free parameter and shifting the gain spectrum to the experimental PL onset, the observed lasing threshold is reproduced for $\Delta E = -1.5 \text{ meV}$ (L7*) and -2.5 meV (L9).

We will show below that we can understand with our model—keeping the values of the parameter the same—the lack of lasing in L10 and L11, but only when considering that the strain dependence of the directness is smaller than anticipated from the TB model [24].

V. LINEWIDTH ANALYSES AND CAVITY LOSS

In Fig. 5(a), we show the linewidth evolution with respect to the excitation power of the L9 cavity modes labelled in Fig. 5(b). The reported linewidths $\Delta(h\nu)$ are apodized. We identify three regimes: (i) The linewidth of modes 1–4 narrows because of the gain. In line with the assumption that lasing occurs at the gain peak, the lasing mode, labeled as 1, narrows the most. (ii) The linewidths of the high-energy modes 5 and 6 are largely independent of the input power. Their values scatter around 0.45 meV. We relate this effect to transparency, as detailed in the next paragraph. (iii) Near and above lasing threshold, the linewidth levels off. The nonlasing modes from 2 to 4 saturate at 0.20 meV. This behavior can be well understood from the Fermi level pinning when lasing occurs.

(iv) Unexpectedly, also the lasing mode 1 does not narrow but saturates at about 0.15 meV, well above the spectral resolution of our experiment. In principle, such behavior could come from mechanical vibrations of the floating nanocavities, which would periodically shift the cavity’s resonant position and thus would lead to a peaked noise spectrum [45]. However, the noise spectrum observed for L7* when lasing is found to be flat. We thus attribute the finite laser linewidth to refractive index fluctuation induced by the carriers in the L-valley and multimode lasing on nearly degenerate modes; cf. Sec. VII.

Via the observation of (ii), we gain access to cavity loss. In line with our Fig. 4(b) gain calculation, a wide transparency band (i.e., zero absorption) occurs for transitions with energies above the gain region. We make use of this characteristic behavior and translate the 0.45 meV linewidth of modes 5 and 6 into a cavity loss α_c . From $\Delta\nu = 1/(2\pi\tau)$, where τ is the photon decaying time, equal to $\tau = n_g/(c\alpha_c)$, where n_g is the group refractive index, we get $\alpha_c \approx 103 \text{ cm}^{-1}$. This procedure is well supported by the observation that all samples, save the highest strained sample L11, have high-energy mode linewidths saturating at about 0.45 meV. Intrinsic material losses, such as the parasitic free carrier and IVB absorption, are largely negligible at high energies, in line with our model.

From the standard threshold condition, $\exp(\Gamma_{xy}g_{th}l_b)\exp(-\alpha_c l_c)\exp(-\Gamma_{xy}\alpha_m l_b) = 1$, where $\Gamma_{xy} = 0.94$ is the transversal confinement factor, g_{th} is the material gain at threshold, $l_b = 8 \mu\text{m}$ is the active material length, and $l_c = 44 \mu\text{m}$ is the length of the cavity, we can deduce that the active material delivers at threshold a gain of $g_{th} = \Gamma_{xy}^{-1}\alpha_c l_c/l_b + \alpha_m$.

The gain required to start lasing is thus quite significant due to the low filling factor $\Gamma_{xy}l_b/l_c = 0.17$ of the active material. Even without any material loss, the necessary gain for lasing is thus 600 cm^{-1} .

The differential gain is obtained via the slope of the linewidth narrowing starting from transparency up to the excitation power corresponding to a reference density of $N_r = 10^{18} \text{ cm}^{-3}$. Up to this density, the IVB absorption increase is linear. We consider the mode showing the strongest

TABLE II. Band offset ΔE of undoped and phosphorus-doped samples obtained from the laser threshold (LD), the differential linewidth (DL), and the linewidth comparison (LC) to L9 as outlined in the main text, in comparison to tight-binding (TB) model calculations. The differential linewidths obtained from the experiments shown in Figs. 5, 7, and 14 are included in parentheses.

Method \ Samples		Undoped					
		L5	L6	L7*	L9	L10	L11
LD				-1.5 meV	-2.5 meV		
DL		3.0 meV	2.0 meV	-1.0 meV	-2.0 meV	-4.0 meV	-6.0 meV
(measurement)		(-38 meV/W)	(-47 meV/W)	(-70 meV/W)	(-80 meV/W)	(-96 meV/W)	(-116 meV/W)
LC						-4.0 meV	-5.0 meV
TB model		4.8 meV	1.7 meV	-2.3 meV	-4.9 meV	-9.7 meV	-14.5 meV

Method \ Samples		Doped	
		Low: $1.8 \times 10^{18} \text{ cm}^{-3}$	High: $6.3 \times 10^{18} \text{ cm}^{-3}$
DL		-6.5 meV	< -10 meV
(measurement)		(-133 meV/W)	(< -200 meV/W)

reduction, which is obviously the lasing mode for L7* and L9. For the latter, this is shown as a dashed light-blue line in Fig. 5(a). We then convert the slope to the differential net gain using the linewidth definition in units of energy $\Delta(h\nu) = hc\alpha/(2\pi n_g)$. For L9, we find $dg/dN = 4.33 \times 10^{-16} \text{ cm}^2$, which is close indeed to the calculated value of $g(N_r)/(N_r - N_0) = 4.70 \times 10^{-16} \text{ cm}^2$, as obtained for the offset value of $\Delta E = -2.5 \text{ meV}$ derived by correlating the calculated to the measured N_{th} . N_0 corresponds to the carrier density at transparency. Moreover, for L7*, the offset value determined from the linewidth/gain analyses is in close agreement with ΔE obtained from threshold density analyses. These conformities give confidence in the slope based offset determination of the nonlasing samples, L5, L6, L10, and L11. Values are given in Table II together with the deduced linewidth reduction per mW of excitation. The corresponding linewidth analyses for L9, L10, and L11 are detailed in Appendix F, together with the linewidth excitation dependence obtained for these samples at $T = 30 \text{ K}$. To circumvent possible issues because the gain may increase nonlinearly near transparency, in particular for L10 and L11, the excitation density corresponding to a reference linewidth value of L9 is used for an alternative offset determination. Again, the resulting offsets—cf. Table II—are in close agreement with the ones based on the slope method. For an overview of the three methods to obtain the ΔE from the threshold and/or the experimental linewidth reduction, we refer the reader to Appendix G.

While the experimental offset values agree among each other, the comparison to the model is striking. First, by interpolation of ΔE between L6 and L11, we obtain that the crossover occurs for a uniaxial tensile strain of 6.05%. This is in excellent agreement with the model. In contrast, the dependence of the offset on strain differs considerably: we obtain that the experimental slope is smaller than predicted by almost a factor of 2. The slope determination may be (i) affected by the simplifications made in the modeling of gain and IVB absorption, or (ii) impacted by technical issues, such as material quality imperfection or bridge distortion, which

may introduce a nonuniaxial component of stress. We address some of these points in Appendix I. In principle, of course, it would also be possible (iii) that the theory is inaccurate with respect to the slope. To prove this, the offset would have to be measured not only near the crossing at around 6% of strain, but also at medium strain, about 3%. Photoreflexion measurements [46] could be the most suitable method here. Despite these unresolved discrepancies between experiment and model, we are confident about the determination of the crossover, since it is based on the observation of lasing at low temperatures. The crossover determination by means of the analysis of the temperature dependence of the PL intensity—as presented in Ref. [47] for the case of strained Ge—thus turns out to be inaccurate in retrospect.

VI. N-DOPING

We now examine the PL of strained microbridge cavities made of *in situ* doped Ge, with phosphorus (P) concentrations of 1.8 and $6.3 \times 10^{18} \text{ cm}^{-3}$. We refer to these samples as low doping (LD) and high doping (HD) samples, respectively. The strain, as inferred from the onset of the PL, is about 5.8%, similar to that of the undoped microbridge sample L6. PL results are shown in Figs. 6(a) and 6(b). The doped samples do not lase. However, compared to the spectra of L6 shown in Fig. 2, cavity modes already develop at low power, and the lines narrow fast with the excitation power; cf. Fig. 6(c). However, as the linewidth saturation also sets in already at low power, both doped samples seem far from reaching the lasing threshold. Lasing seems even further away than for L6, as found by comparing the LD and HD spectra at the highest power in Figs. 6(a) and 6(b) and the corresponding one shown in Fig. 2(b).

The linewidth slope method yields an offset for both doped samples that is negative, namely -6.5 and -10 meV , respectively. In fact, for the higher doped sample, the slope shown in Fig. 6(c) is only a lower limit, as the linewidth was already of 0.3 meV at 2 mW excitation. Thus, compared to the 2.0 meV offset for L6, phosphorus doping seems to reduce

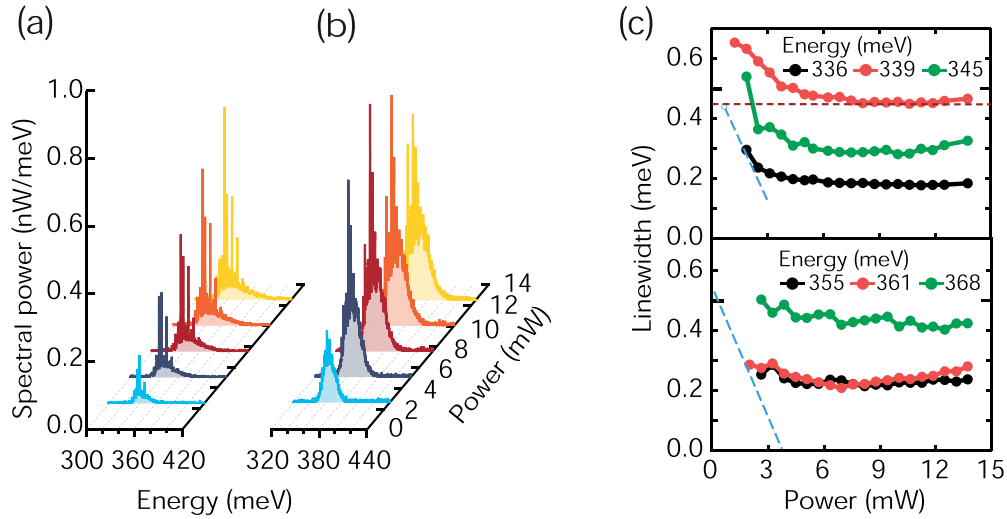


FIG. 6. Power-dependent photoluminescence spectra at 15 K of equally strained Ge:P cavities with (a) $N_d = 1.8 \times 10^{18} \text{ cm}^{-3}$ and (b) $N_d = 6.3 \times 10^{18} \text{ cm}^{-3}$. (c) Up and down panel compare the linewidth dependence on the excitation power of the LD and HD samples, respectively. The dashed lines represent the linewidth slope used for the ΔE determination.

ΔE by about 8.5 meV and more than 12 meV for the LD and HD samples, respectively. Interestingly, these numbers are in reasonable agreement with the Fermi level positions in the L conduction band of the LD and HD samples, namely 8.4 and 20 meV, respectively.

We thus seem to have obtained by n -doping a system that becomes quasidirect, as we determine offset values that are negative. However, for higher excitation, the gain does not develop further and thus it does not overcome the optical loss, particularly in the high doping case. The most likely explanation for the reduction of the gain at high excitation is a strong reduction of the lifetime caused by the Auger effect. This explanation is consistent with the observation of the positions of the cavity modes, which shift more and more slowly for the doped samples at increasingly higher excitation density. Alternatively, the gain may not be pure interband, but it may be related to donor- to valence-band transitions that change their character from L to Γ when the two conduction bands align. Such band tail states [48] may give a weak but insufficient gain.

VII. LASER LINEWIDTH

For the characterization of the laser linewidth, we focus on sample L7*. The laser resonance of L9 overlaps with an absorption band in air which complicates the linewidth analyses. Examples of the measured laser line spectra of L7* are shown in Appendix H, together with the fit function that consists of Lorentzian broadened lines.

For the discussion, we follow the standard model of Schawlow-Townes (ST) [40], which describes the linewidth of a single-mode laser above threshold as $\Delta\nu = \eta_{ST}(1 + \alpha^2)/P_{out}$, where P_{out} is the radiated power per round trip. The factor η_{ST} depends on the amount of gain at threshold, the cavity loss, and the degree of population inversion [40]. The linewidth enhancement factor α describes the coupling between intensity and phase noise [49]. The $\Delta\nu$ value is notably governed by the fact that above threshold, gain

clamping fixes the amount of carrier density to N_{th} , thereby stabilizing the spontaneous emission and thus the random drift of the phase.

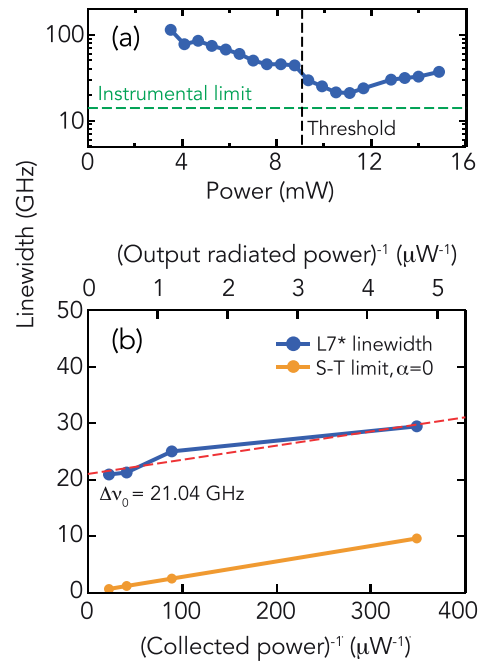


FIG. 7. Experimental linewidth of the L7* lasing mode (blue). (a) Linewidth as a function of excitation power. The instrumental resolution at 15 GHz is indicated in green. (b) L7* linewidth as a function of the inverse of the collected power when the sample is operated above threshold but before the rollover. The red dashed line is a linear fit to the experiment, yielding a residual linewidth $\Delta\nu_0$ of about 21 GHz. In yellow: linewidth of the standard model of Schawlow Townes for $\alpha = 0$ as obtained from the estimated radiated output power given on the upper scale. It is deduced from the collected power as described in the text.

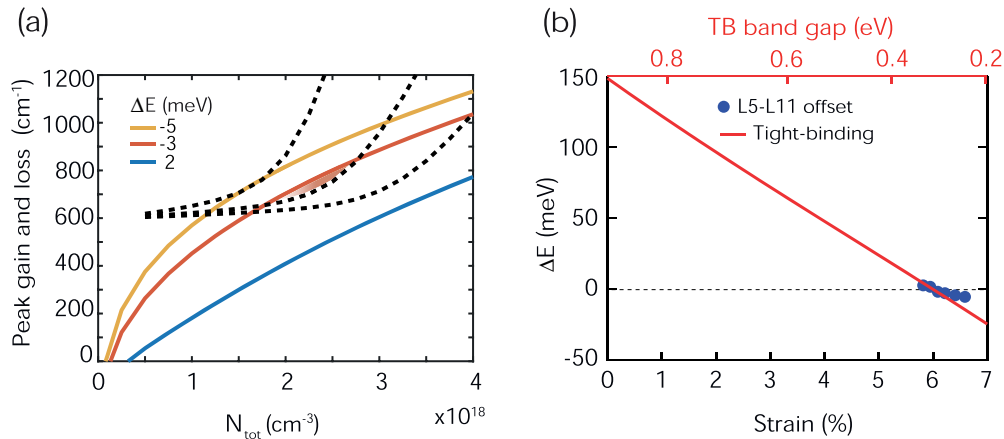


FIG. 8. (a) Peak optical gain as a function of the total carrier density up to $4 \times 10^{18} \text{ cm}^{-3}$ for the approximated energy difference ΔE of L6, L9, and L11. For L9 and L11 we choose the more accurate values obtained with the threshold and linewidth reference methods, respectively (cf. Appendix G). The overall loss due to cavity loss and parasitic intervalence band absorption is shown as a black dashed line. It was extracted from Fig. 4(c). (b) Energy difference ΔE as a function of uniaxial strain at low temperature. Red denotes the prediction from the tight-binding theory, while blue dots show the experimental points extracted from Table II. The upper axis converts via the tight-binding model the strain to the Γ -VB1 transition energy.

Figure 7 (top panel) shows the measured linewidth—below and above threshold—as a function of the excitation power. On the lower panel, the laser linewidth is shown as a function of the inverted collected power. When lasing starts, the linewidth is inversely proportional to the output power, as predicted by the theory. In contrast to theory, however, the experimental linewidth remains finite, and it approaches a residual value $\Delta\nu_0$ of about 21 GHz, i.e., 0.09 meV, whose interpretation we give in the next paragraph. Before, we estimate the α value from the linewidth dependence on the power by converting the collected power to the total output radiated power P_{out} ; cf. the upper scale of the lower panel of Fig. 7. The conversion is calculated from the corner cube far-field emission pattern as explained in [1]. We thus obtain that the linear increase is reproduced by the ST model for the case of $\alpha = 0$ and the parasitic loss as shown in Fig. 4(c). A low value for α means that the change in carrier density does not change the absorption but rather the peak gain. This is not exactly what we find from the gain calculation shown in Fig. 4(b), which results in an α value of about 1.7. This value is indeed smaller than what is found for truly direct-band-gap systems, such as III-V compounds, where α values are between 2 and 6.

While different experiments validated the Schawlow-Townes theory [50–52], it was often observed that the linewidth of semiconductor lasers was limited by a power-independent contribution $\Delta\nu_0$ [53–59]. The origin of the power-independent contribution is still debated. It is often attributed to noise, which adds to the quantum noise, like $1/f$ noise [60,61] or occupation fluctuation noise [62]. However, in those cases the linewidth saturates at values in the range of 1–10 MHz, orders of magnitude lower than in our case.

A much stronger broadening mechanism is refractive index fluctuations induced by carrier number noise. This effect, usually neglected thanks to gain clamping, is relevant in injection-controlled tuneable-wavelength lasers, as studied in [63,64]. We apply this carrier noise model to the strained germanium laser, where most of the carriers are not optically

active because they populate the L valley and are thus not clamped by gain. From [63,64] adapted to our case, we obtain a $\Delta\nu_0$ value of 3.6 GHz; cf. Appendix H. The remaining quantitative discrepancy we attributed to multimode operation, which is not included in the ST model. Indeed, we observe a line doublet, cf. Appendix H, separated in frequency by about 26 GHz.

VIII. DISCUSSION

The most remarkable observation of the current investigation concerns the existence of a sweet spot of strain at which lasing occurs. This surprising experimental result can be reproduced by the model as demonstrated in Fig. 8(a), which gives the peak gains as functions of total carrier densities for samples L6, L9, and L11. For the calculation of the gain, we used the experimental values for ΔE reported in Table II. Superimposed, we show the total loss due to cavity loss and intervalence band absorption. As before, the IVB absorption is calculated for the energy where the gain peaks. We thus obtain that L5 and L6 do not reach the threshold due to the low amount of delivered gain and the fast rise of IVB absorption for densities larger than 2 to $3 \times 10^{18} \text{ cm}^{-3}$. In contrast, the gain increases fast enough in L9 (and also L7 as well as L7*) to reach the lasing threshold at about $2 \times 10^{18} \text{ cm}^{-3}$. The onset of the IVB absorption explains the observed breakup of lasing at high excitation shown in Fig. 4(a). Finally, L11 does not reach the threshold because strong parasitic loss occurs just before the gain is large enough to overcome the optical losses. As shown in Fig. 4(d), the temperature dependence of the lasing is—at least qualitatively—well explained by the model with phenomenological temperature and broadening parameters. Figure 8(b) shows that the experiment and theory are definitely in line concerning the crossing to a direct-band-gap configuration, but not in the slope, which is shallower in the experiment. We have argued that our method is more accurate for determining the crossover than for determining the slope.

The indirect-to-direct crossover determined here also confirms the results from Ref. [1] where samples, similar to those investigated here, strained up to 5.9%, thus with an indirect band gap, were studied. Samples of Ref. [1] showed lasing at low temperature, but only upon pulsed excitation, with a pulse length of 100 ps. This was attributed to (i) indirect band gap, i.e., $\Delta E > 0$, and (ii) the buildup of a transient population inversion, thanks to the blocking of the phonon-mediated Γ to L intervalley scattering. Such a process is particularly effective for electrons with excess energy lower than 28 meV, which corresponds to the energy of the zone-boundary longitudinal acoustic phonon. As a matter of fact, the offset ΔE of the least strained samples showing lasing and the most heavily loaded samples showing no lasing of Ref. [1] are indeed less than 20 meV and about 28 meV, according to the TB calculation for strain of 5.4% and almost 5%, respectively.

IX. CONCLUSION

We developed a versatile laser analysis method for determining the gain and the material and optical losses of group-IV lasers. It is made by deriving the values for the injection carrier densities and the cavity losses from the measurement of the refractive index change and the mode linewidth, respectively. We exemplified the method using Ge microbridges strained up to 6.6%.

We determined the strain required to lift germanium across the transition from an indirect to a direct band structure by comparing the calculated gain and loss with experimental observations of laser threshold and/or differential gain. We found a sweet spot for the lasing threshold for uniaxial tensile strain of approximately 6.1%, which also marks the crossover to a direct-band-gap semiconductor. At lower strain, the optical gain is too low to overcome cavity losses, while samples at higher strain suffer from IVB absorption, which depends critically on the transition energy, excitation strength, and temperature. The obtained crossover is well predicted by the tight-binding model [24] and confirms the transient blocking of the valley scattering model of Ref. [1]. The experimental slope by which the offset changes is, however, smaller than predicted. The adoption of an optimized cavity, like a distributed Bragg reflector as in [65], might extend the strain and temperature ranges where lasing is achieved, enabling future studies to address whether the ΔE disagreement is of a fundamental or experimental nature.

Our method revealed that doping brings about a slight gain enhancement, but only at low excitation, which we attribute to (i) additional gain from doping-induced band tail states, and (ii) a reduced lifetime due to Auger scattering.

We discussed the fundamental physics of the laser linewidth in the case when carriers fill dominantly the L levels, which are not optically active and thus are not clamped by gain. We expect that such L-carrier fluctuations may also play a role in other group IV lasers, depending on the actual offset and the temperature of the laser.

Altogether, we have shown a practical way to achieve lasing in Ge at low temperature and in steady state. We related the lasing to the crossover to a direct band gap. Our analytic method can be applied perfectly to laser cavities realized with other material systems such as GeSn alloys, hexagonally

ordered SiGe [66], and defective Ge [67]. It could thus greatly accelerate the future development of group IV lasers for integration into Si microelectronics.

ACKNOWLEDGMENTS

This work was funded in part by the Swiss National Science Foundation SNF (Grant No. 200021_162658) and the CEA-Grenoble program Phare Photonics. The authors acknowledge the assistance of the staff of CEA Leti clean rooms and CEA Advanced technological platform PTA, as well as the technical support for the experiments performed at PSI from Stefan Stutz.

APPENDIX A: ROOM-TEMPERATURE PL INVESTIGATION

Figure 9(a) compares the experimental values of the Γ -VB1 transition energy at room temperature with model predictions for various strain levels. The red and green give the value of the tight-binding (TB) [1,24] and the deformation potential [68] models, respectively. The solid and dashed lines refer to the Γ -VB1 and L-VB1 transitions, respectively. Predictions are compared with experimental results for samples with strains determined by Raman scattering. Black circles show the values inferred from the work of Guilloy *et al.* [22], showing a good agreement up to 3.3% with the TB prediction of the Γ -VB1 transition. The validity of the TB model is further confirmed up to 4.2% by the values highlighted in blue, extracted from the photoluminescence measurements of samples L9, L10, and L1, as shown in Fig. 9(b).

Samples L9, L10, and L11 are strained at 3.98%, 4.10%, and 4.23%, respectively. As for the measurements taken at low temperature, the band-gap position is estimated as the energy corresponding to the half-maximum spectral intensity of the photoluminescence background; cf. Fig. 9(b). The spectral features between 450 and 490 meV are attributed to absorption in air. The emission is suppressed at high energy by a long pass filter cutting below (above) 2440 nm a wavelength (508 meV). The low-energy side of the photoluminescence of Fig. 9(b) is impacted by the tail of the thermal background.

APPENDIX B: COMPARISON BETWEEN SAMPLES L7 AND L7*

Figure 10(a) shows PL spectra of an L7 sample from chip A and a selected L9 sample from chip B, with excitation intensity below the laser threshold. Except for the intensity—which we attribute to a detector misalignment for the case of sample L7—the spectra look very similar, with an onset at the same energy of about 300 meV. The latter indicates that both samples are loaded with approximately the same strain. Moreover, considering that all the investigated samples have identical optical cavities and thus differ only by their amount of strain, the equal laser threshold, cf. Fig. 10(b), further indicates the match between this sample pair. Therefore, to enable measurement sequences on the same chip B not only for samples L9, L10, and L11, we decided to include also this specific L9 cavity in our study, and we denote it as L7*.

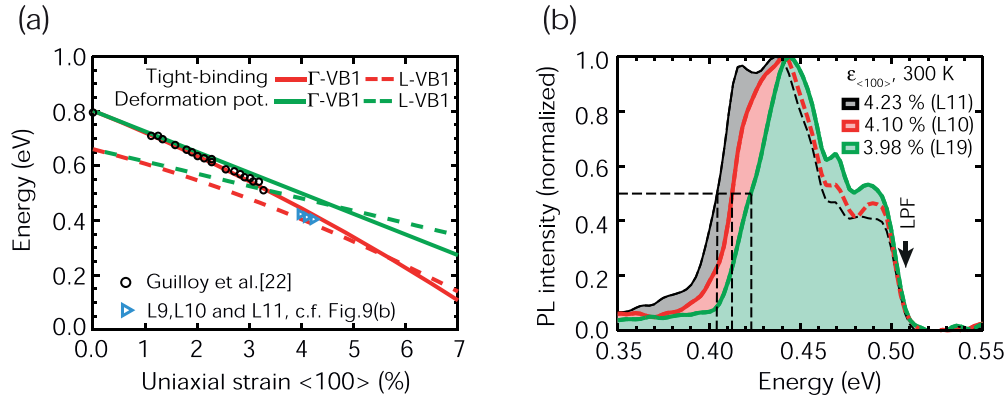


FIG. 9. (a) Interband transition energies in Ge, for uniaxial strain along one of the equivalent crystallographic directions $\langle 100 \rangle$ at 300 K. Solid lines refer to the Γ -VB1 transition, while dashed lines refer to the indirect transition L-VB1. Energies from the tight-binding and deformations potential models are in red and green, respectively. Experimental values are inferred from [22]. (b) Low-resolution photoluminescence measurement at 300 K upon continuous-wave excitation running at 590 meV of samples L9, L10, and L11. The high-energy PL is blocked by a lowpass filter (LPF).

APPENDIX C: CAVITY MODE SHIFT

The refractive index change Δn caused by the injected carrier N is described in the Drude-based model [69] as

$$\Delta n = -\frac{q^2 \mu_0 \hbar^2 c^2}{2n_g (h\nu_{\text{mode}})^2 m_0 \mu_{\text{plasma}}} N, \quad (\text{C1})$$

where $h\nu_{\text{mode}}$ is the photon energy of the considered cavity mode, μ_0 is the vacuum permeability, n_g is the unperturbed material group refractive index of 4.5, and μ_{plasma} is the plasma mass of 0.06. We calculate the energy shift of the cavity mode from the relation $\Delta h\nu/h\nu = -\Delta n/n$ and by considering transversal and longitudinal fundamental mode confinement factors of $\Gamma_{xy} = 0.94$ and $\Gamma_z = l_b/l_c = 8/44$, respectively.

In Fig. 11 we report that the cavity mode shifts at 15 K of L6, L7*, and L11 as functions of the excitation power. On the upper scale, we give the carrier concentration as calculated from the Drude model of Eq. (C1). It appears that the thus obtained conversion factor of $0.25 \times 10^{18} \text{ cm}^{-3}/\text{mW}$ is roughly the same in all the investigated samples, indepen-

dently of the temperature (between 15 and 30 K). For the *in situ* phosphorus-doped samples (not shown here), the match is only at low carrier densities.

APPENDIX D: OPTICAL GAIN MODELING

The absorption coefficient is calculated as the ratio between the net photon number absorbed per second per volume unit and the photon number incident per second per area unit. By means of Fermi's golden rule, we calculate the net rate of photon absorption per unit of volume. We then obtain the following expression integrated in the reciprocal space for the absorption of the photon energy $\hbar\omega$ [26]:

$$\alpha(\hbar\omega) = \frac{\pi q^2}{n_r c \varepsilon_0 m_0^2 \omega} \int \frac{2 d^3 k}{(2\pi)^3} |\hat{e} \cdot p_{if}|^2 \times \delta(E_f - E_i - \hbar\omega) [f_v(E_i) - f_c(E_f)], \quad (\text{D1})$$

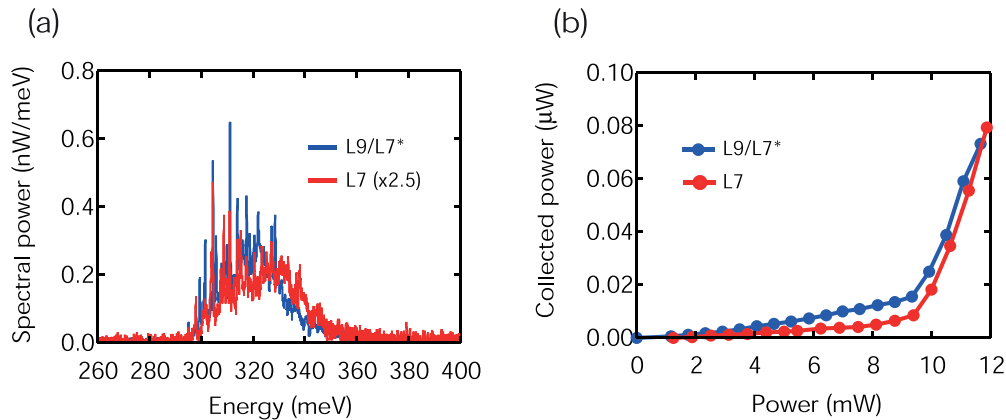


FIG. 10. (a) PL spectra of samples L7 (in red) from chip A and a selected L9 (in blue) from chip B, referred to as L7* in the main text, taken at 15 K and an excitation power of about 6.3 and 6.4 mW, respectively. The spectrum of L7 is enhanced by a factor 2.5 for comparison. (b) PL power as a function of the excitation power at 15 K.

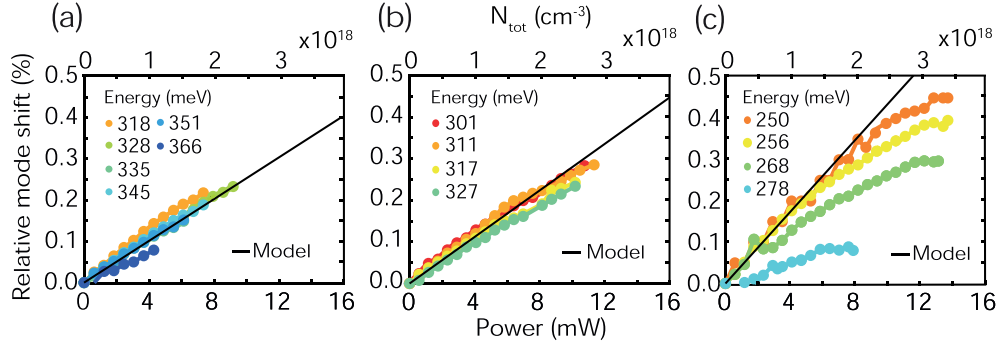


FIG. 11. Relative mode shift $\Delta h\nu/h\nu$ of samples (a) L6, (b) L7*, and (c) L11 at 15 K as a function of the excitation power. The carrier density, given on the upper scale, is calculated from the mode shift according to the Drude model, shown by the black line.

where E_i and E_f are initial and final energies of the interband transition. The carrier statistics is described by the Fermi distribution function:

$$f(E, T, \mu) = \frac{1}{\exp\left(\frac{E-\mu}{k_b T}\right) + 1}, \quad (D2)$$

where μ is the quasi-Fermi level, and by the three-dimensional density of states:

$$\rho^{3D}(E, E_0, m^*) = \frac{1}{2\pi} \frac{(2m^*)^{3/2}}{\hbar^3} \sqrt{E - E_0}. \quad (D3)$$

The quasi-Fermi levels are obtained self-consistently by inverting the charge-neutrality equation: $N_{el} = N_h = N_{tot}$ and assuming thermal equilibrium at temperature T . The electron and hole densities are obtained by integration over both conduction bands (L and Γ) and the three valence bands, respectively:

$$N_{tot}^{el} = \int_{\min(E_\Gamma, E_L)}^{\infty} \sum_{i=\Gamma, L} \rho_i^{3D}(E, E_i, m_i^*) f_c(E, T, \mu_c) dE \quad (D4)$$

and

$$N_{tot}^h = \int_{-\infty}^{E_{HH}} \sum_{i=VB1, VB2, VB3} \rho_i^{3D}(-E, -E_i, m_i^*) \times [1 - f_v(E, T, \mu_v)] dE. \quad (D5)$$

TABLE III. Longitudinal and transverse masses at 6% of uniaxial tensile strain along [001] for the Γ and L bands and for the three valence bands VB1, VB2, and VB3. The values are calculated using the tight-binding model and are expressed in units of m_0 .

Band	E_i (eV) @20 K	m_i^l	m_i^t
Γ	0.314	0.033 29	0.018 13
L	0.314	1.555 67	0.090 67
VB1	0	0.179 87	0.027 63
VB2	-0.160	0.125 04	0.041 92
VB3	-0.777	0.037 15	0.231 03

Table III gives the effective masses and the band edges calculated by means of the tight-binding model for 6% of strain, corresponding to $\Delta E = 0$ meV. m^l is the component longitudinal to the strain, i.e., along [001], while m^t is the component along [100] and [010]. For the L band, m^l and m^t are the component along the [111] and [1-10] directions, respectively.

Table IV gives the dipole matrix elements calculated from the tight-binding model for 6% of strain. The selection rules make no distinction between light TE and TM polarized propagating along the strain direction.

The following approximations were used for the gain calculation: (i) For all strain, we used the dipole matrix element and the masses as given above. (ii) The band dispersion was treated as quadratic because the probed range of \mathbf{k} around the Γ point is small. (iii) Electron-electron and electron-phonon processes were not considered. (iv) Thermal equilibrium was assumed.

Figure 12 shows the contour map of the peak gain as a function of the total carrier density and energy offset ΔE , calculated using the formulation described above. The effective carrier temperature is set to 30 K. The gain spectrum is convoluted with a Lorentzian function with a full width at half-maximum of $\Gamma = 10$ meV, as explained in the main text. When germanium becomes direct, the number of carriers available for optical recombination in Γ , and thus the optical gain, increase strongly, making the gain an excellent probe of the band structure's directness.

APPENDIX E: INTER-VALENCE-BAND ABSORPTION

Figures 13(a) and 13(b) report the IVB absorption spectra for different carrier densities, state broadenings, and

TABLE IV. Dipole matrix elements for transition between the Γ valley and the valence bands for radiation polarized perpendicularly to the strain, calculated with the tight-binding model for 6% of uniaxial tensile strain.

Transition	$ \hat{\mathbf{e}} \cdot \mathbf{p}_{if} ^2$
Γ -VB1	$(m_0/2) \times 11.32$ eV
Γ -VB2	$(m_0/2) \times 10.65$ eV
Γ -VB3	$(m_0/2) \times 0.61$ eV

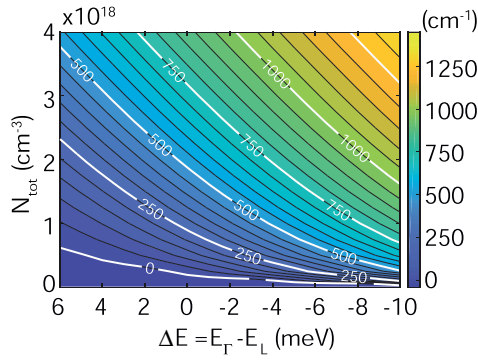


FIG. 12. Contour plot of the optical peak gain for a carrier temperature of 30 K and an optical broadening of 10 meV, as a function of the energy offset ΔE and total carrier density, N_{tot} .

temperatures between 20 and 100 K. Spectra are calculated with the tight-binding model for 6% of strain [24]. The tight-binding valence-band structure and inter-valence-band dipole matrix elements are fed into Eq. (D1), and the integration over the wave vector is performed on a tetrahedral mesh around Γ . The transitions between the upper and the lowest valence bands are neglected because they do not contribute at the strain and transition energies relevant herein. Included, in contrast to the interband case, however, is the nonparabolic band structure and the k -dependence of the matrix elements.

We note that the IVB absorption strongly increases for decreasing energies and peaks at about 160 meV. Moreover, its high-energy tail increases for carrier density above $2 \times 10^{18} \text{ cm}^{-3}$ and temperature $T > 30 \text{ K}$. The latter effect is due to holes filling the states in reciprocal space further apart from the Γ point; cf. Fig. 4(a), main text.

The characteristics of the IVB absorption enable us to interpret qualitatively several of the reported effects (main text), such as the L7* and L9 intensity rollovers that shift to lower powers when the temperature increases. Because the lasing transition energy is lower for L9 than for L7*, the rollover—when the parasitic loss starts dominating—is reached faster for the former. The higher the strain, the lower the band-gap energy and thus the stronger the absorption will be. The gain

increase for L10 and L11 is thus not enough to reach lasing threshold under the present conditions.

We would also like to note that we neglected the free-carrier absorption of electrons (FCA). This process annihilates a photon by exciting an electron from an occupied state below the quasi-Fermi level to an empty state above [70]. Since such a process requires an impurity or a phonon to comply with momentum conservation, the absence of phonons at low temperature makes FCA negligible compared to IVB absorption [71]. It can thus be ignored.

APPENDIX F: L9, L10, AND L11 LINEWIDTH AT 15 AND 30 K

Figure 14 shows the apodized cavity mode linewidth of L9, L10, and L11 at 15 K (a, c, and e) and 30 K (b, d, and f). At the lowest temperature of 15 K, the cavity modes at low energy first narrow because of gain. Later, at higher excitation, they smoothly broaden. We interpret the transition from narrowing to broadening as the moment the differential loss overcomes the differential gain. The power at which the linewidth starts broadening decreases when reducing the cavity mode energy. For L9, L10, and L11 samples, the onset of broadening occurs at about 12, 9, and 4.5 mW, respectively.

At 30 K, the linewidth broadening becomes stronger. Its onset, for L9 and L10 samples, starts at excitation powers of 9 and 7.5 mW, respectively. For the highest strained sample L11, the impact of a temperature increase is less obvious than for L9 and L10. For L11, despite some fluctuations, the onset can be located between 3 and 6 mW, similarly as at 15 K. Comparing the linewidth slope at low power, we observe that gain is largely independent of temperature.

APPENDIX G: LINEWIDTH TO GAIN CONVERSION

Figure 15 shows the peak gain calculated as a function of the total carrier density for different offset values ΔE . The three approaches applied in the main text to probe the strained germanium band structure are indicated as (1) lasing threshold, (2) linewidth reduction or differential gain, and (3) linewidth or gain reference.

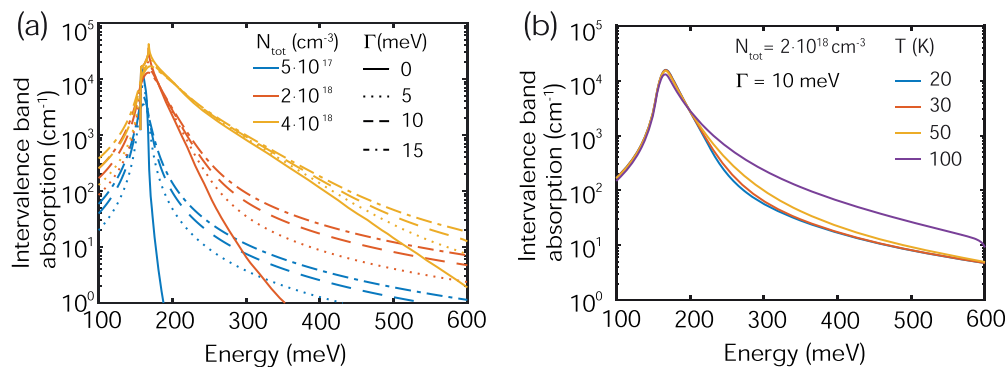


FIG. 13. Intervale band absorption spectra calculated with the tight-binding model for 6% of strain, corresponding to zero-energy difference ΔE , (a) at 30 K for different carrier densities (shown by different colors) and state broadening (line): solid, dotted, dashed, and dash-dotted lines correspond to 0, 5, 10, and 15 meV broadening, respectively, and (b) at $N_{\text{tot}} = 2 \cdot 10^{18} \text{ cm}^{-3}$ and a state broadening of 10 meV for different temperatures. Calculations consider only TE- and TM-polarized light, propagating along the direction of the uniaxial strain.

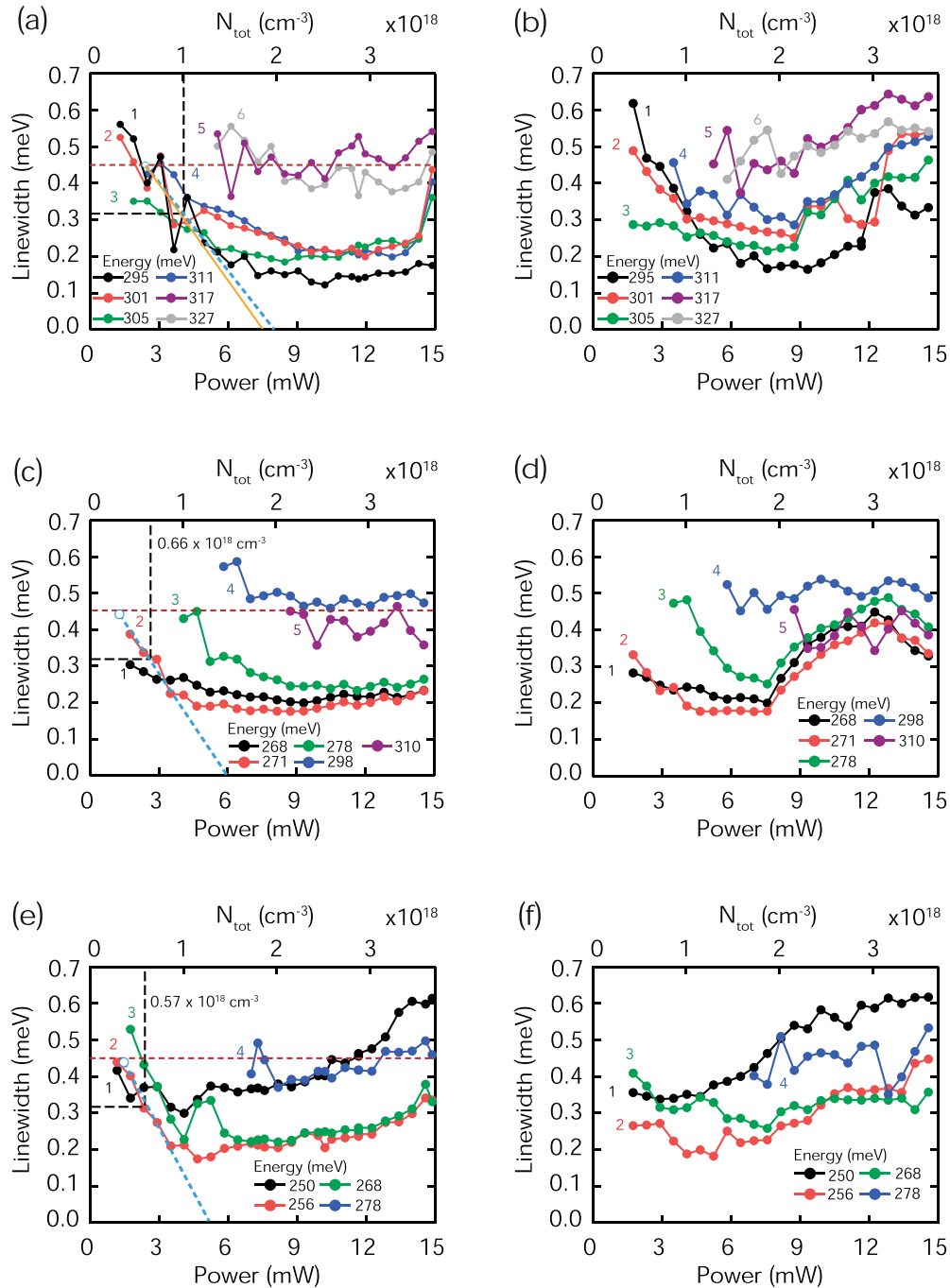


FIG. 14. Linewidth as a function of power and temperature. L9 linewidth at (a) 15 K and (b) 30 K. L10 linewidth at (c) 15 K and (d) 30 K. L11 linewidth at (e) 15 K and (f) 30 K. The black dashed lines in (c) and (e) indicate the carrier density at which the linewidth reaches the value of 0.317 meV, as found for L9 (a) at the reference carrier density of $N_r = 1 \times 10^{18} cm^{-3}$ (cf. text Appendix H). The dashed blue line in (a), (c), and (e) shows the linear regression used to extract the differential gain (see main text).

The label (1) in Fig. 15 depicts the situation, for L9, where the gain overcomes the total losses at the lasing threshold density $N_{th} = 2.1 \times 10^{18} cm^{-3}$. The IVB absorption at the lasing energy of 295 meV and a carrier density of $2.1 \times 10^{18} cm^{-3}$ contributes by about $87 cm^{-1}$ to the total loss of $687 cm^{-1}$. A corresponding gain is reached for ΔE between -2 and -3 meV. To probe nonlasing samples, we follow the narrowing of the linewidth from N_0 to the reference carrier density

$N_r = 1 \times 10^{18} cm^{-3}$ [cf. Figs. 5(a) and 14] and we convert this to the differential net gain. ΔE is obtained by comparing the gain slope to the model, as indicated by label (2), which exemplifies the case of L5. In a first approximation, the IVB absorption at $N_r = 1 \times 10^{18} cm^{-3}$ is neglected. For samples L10 and L11, we also compare the carrier density at which their linewidth reaches the value of sample L9 at $N_r = 1 \times 10^{18} cm^{-3}$. Parity is obtained for densities of 0.66×10^{18}

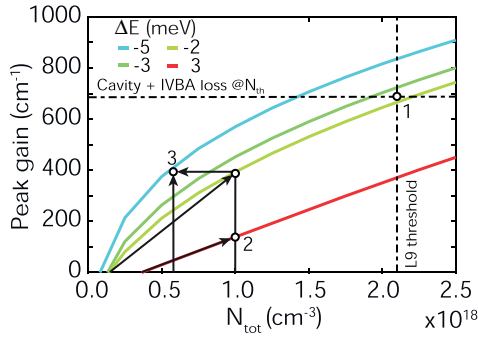


FIG. 15. Peak gain as a function of the total carrier density for various energy offsets ΔE . The purpose of this figure is to illustrate the three methods to determine ΔE , as described in the main text.

and $0.57 \times 10^{18} \text{ cm}^{-3}$, respectively, cf. Figs. 14(d) and 14(f). Label (3) in Fig. 15 exemplifies the case of L11.

APPENDIX H: LASER LINewidth OF L7*

Figure 16 shows L7* nonapodized lasing spectra for excitation powers ranging from 9.90 to 11.07 mW at 15 K. The fitting function suggests the presence of two modes separated by about 0.08 meV. For the linewidth analyses, we have used the linewidth of the strongest mode.

To evaluate the power-independent contribution $\Delta\nu_0$ due to noise of the unclamped carrier population in L, we recall the excess linewidth expression developed for the wavelength-tunable lasers [33,34]:

$$\Delta\nu_0 = \frac{q I_t}{\pi} \left(\frac{\Delta\omega_{e, \text{mode}} \tau}{q} \right)^2, \quad (\text{H1})$$

where I_t expresses the injection tuning current, $\Delta\omega_{e, \text{mode}}$ is the lasing angular frequency change per unit of charge q , and τ is the electron state lifetime. We apply the above equation to the strained germanium laser case by expressing I_t as $P_{\text{abs}}/(h\nu_{\text{ext}})$, where P_{abs} is—as above—the amount of power absorbed by the microbridge, and $h\nu_{\text{ext}}$ is the excitation energy of 0.59 eV converted in Joule units. At the threshold of 9.6 mW, $P_{\text{abs}} = 0.38 \text{ mW}$. We assume that all the carriers populate the L valley. As the change of angular frequency is related to the change of refractive index via the relation $\Delta\omega/\omega = -\Delta n/n$, we can express the change per carrier from the Drude

model [69] as already used in Appendix C:

$$\begin{aligned} \Delta\omega_{e, \text{mode}} &= -\frac{\omega_{\text{mode}}}{n} \frac{\Delta n}{NV} \\ &= \omega_{\text{mode}} \frac{q^2 \mu_0^2 \hbar^2 c^2}{2(n \hbar \omega_{\text{mode}})^2 m_0 \mu_{\text{plasma}}} \frac{1}{V} \\ &= 3.39 \times 10^5 \frac{\text{rad}}{\text{s}}, \end{aligned} \quad (\text{H2})$$

where N , μ_0 , μ_{plasma} , and n_g , are as defined in Appendix C. The volume of the strained microbridge V is $8 \times 10^{-12} \text{ cm}^{-3}$, while $\hbar\omega_{\text{mode}}$ is the photon energy of 0.311 eV. By inserting Eq. (H2) into (H1), and by using a carrier lifetime of 5 ns, as discussed in Appendix C, we obtain a linewidth broadening of about $\Delta\nu_0 = 3.6 \text{ GHz}$. From the experiment, we obtain $\Delta\nu_0 = 21 \text{ GHz}$.

The remaining discrepancy is attributed to the fact that our laser does not operate in single mode. For such nonideal single-mode or multimode lasers, the power-independent contribution to the linewidth can reach values above the GHz level due to a nonlinear coupling between modes [72].

APPENDIX I: ADDITIONAL CONSIDERATIONS TO EXPLAIN THE WEAK DEPENDENCE OF THE OFFSET ON STRAIN

Here we shall consider three experimental and technical issues that could explain the shallow evolution of offset energy with strain.

(i) An unintentional misalignment of the bridge structures with respect to $\langle 100 \rangle$ would increase ΔE for a given strain. However, the error margin of our alignment tool, $< 1^\circ$, is too small to have an impact, making this explanation rather unlikely.

(ii) A similar possibility concerns an inhomogeneous strain distribution as the microbridge structure may bend out of plane. Such bending evokes shear stress, which would have an impact on strain. We indeed observe that the expected relationship between the length of the pads and the bridge and their transversal dimensions does not apply for samples with strains larger than in L6. This is why we determined the strain from the measured band-gap energy, and we did not use its correlation to the geometry, as previously demonstrated [1].

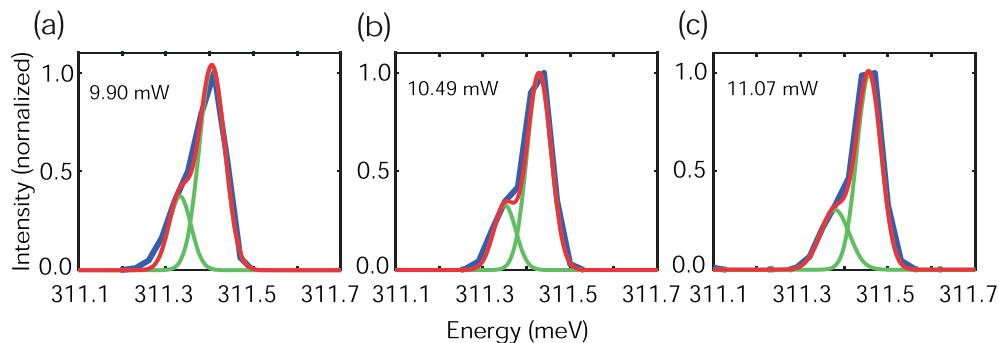


FIG. 16. (a) In blue the nonapodized L7* lasing spectra at 15 K for an excitation power of (a) 9.90 mW, (b) 10.49 mW, and (c) 11.07 mW. The fitting function in red is the sum of two Voigt functions (green).

However, shear stress is expected to be minor in the bridge also in the case of bending.

(iii) A degradation of the samples' optical properties at the highest strain, for example, due to the generation of a parasitic recombination channel, could result in a gain not evolving as expected. We indeed find that the PL inten-

sity is reduced for samples L10 and L11 compared to the others. However, since—at low excitation strength—the dependence of the charge density on the excitation power is not impacted by strain as obtained from the shift of cavity modes, an upcoming nonradiative recombination path can be excluded.

-
- [1] F. T. Armand Pilon *et al.*, Lasing in strained germanium microbridges, *Nat. Commun.* **10**, 2724 (2019).
- [2] S. Wirths *et al.*, Lasing in direct-bandgap GeSn alloy grown on Si, *Nat. Photon.* **9**, 88 (2015).
- [3] O. Moutanabbir *et al.*, Monolithic infrared silicon photonics: The rise of (Si)GeSn semiconductors, *Appl. Phys. Lett.* **118**, 110502 (2021).
- [4] D. Stange *et al.*, Optically pumped GeSn microdisk lasers on Si, *ACS Photon.* **3**, 1279 (2016).
- [5] V. Reboud *et al.*, Optically pumped GeSn micro-disks with 16% Sn lasing at 3.1 μm up to 180 K, *Appl. Phys. Lett.* **111**, 092101 (2017).
- [6] N. von den Driesch *et al.*, Advanced gesn/sigesn group IV heterostructure lasers, *Adv. Sci.* **5**, 1700955 (2018).
- [7] D. Stange *et al.*, GeSn/SiGeSn heterostructure and multi quantum well lasers, *ACS Photon.* **5**, 4628 (2018).
- [8] Y. Zhou *et al.*, Optically pumped GeSn lasers operating at 270 K with broad waveguide structures on Si, *ACS Photon.* **6**, 1434 (2019).
- [9] J. Chrétien *et al.*, GeSn lasers covering a wide wavelength range thanks to uniaxial tensile strain, *ACS Photon.* **6**, 2462 (2019).
- [10] A. Elbaz *et al.*, Ultra-low-threshold continuous-wave and pulsed lasing in tensile-strained GeSn alloys, *Nat. Photon.* **14**, 375 (2020).
- [11] Y. Zhou *et al.*, Electrically injected GeSn lasers on Si operating up to 100 K, *Optica* **7**, 924 (2020).
- [12] A. Elbaz *et al.*, Reduced lasing thresholds in GeSn microdisk cavities with defect management of the optically active region, *ACS Photon.* **7**, 2713 (2020).
- [13] A. Bjelajac, M. Gromovyi, E. Sakat, B. Wang, G. Patriarache, N. Pauc, V. Calvo, P. Boucaud, F. Boeuf, A. Chelnokov, V. Reboud, M. Frauenrath, J. Hartmann, and M. El Kurdi, Up to 300 K lasing with GeSn-On-Insulator microdisk resonators, *Opt. Express* **30**, 3954 (2022).
- [14] J. Chrétien, Q. M. Thai, M. Frauenrath, L. Casiez, A. Chelnokov, V. Reboud, J. M. Hartmann, M. Kurdi, N. El Pauc, and V. Calvo, Room temperature optically pumped GeSn microdisk lasers, *Appl. Phys. Lett.* **120**, 051107 (2022).
- [15] H.-J. Joo *et al.*, 1D photonic crystal direct bandgap GeSn-On-Insulator laser, *Appl. Phys. Lett.* **119**, 201101 (2021).
- [16] Z. C. Wang, B. Tian, M. Pantouvaki, W. M. Guo, P. Absil *et al.*, Room-temperature InP distributed feedback laser array directly grown on silicon, *Nat. Photon.* **9**, 837 (2015).
- [17] S. Chen *et al.*, Electrically pumped continuous-wave III-V quantum dot lasers on silicon, *Nat. Photon.* **10**, 307 (2016).
- [18] Y. Wan, S. Liu, C. Shang, R. W. Herrick, and W. W. Chow, A review of high performance quantum dot lasers on silicon, *IEEE J. Quantum Electron.* **55**, 2000511 (2019).
- [19] M. Rio Calvo, L. Monge Bartolomé, M. Bahriz, G. Boissier, L. Cerutti, J. Rodriguez, and E. Tournié, Mid-infrared laser diodes epitaxially grown on on-axis (001) silicon, *Optica* **7**, 263 (2020).
- [20] Z. Lohmari *et al.*, InAs-based quantum cascade lasers grown on on-axis (001) silicon substrate, *APL Photon.* **5**, 041302 (2020).
- [21] S. Gupta, D. Nam, J. Vuckovic, and K. Saraswat, Room temperature lasing unraveled by a strong resonance between gain and parasitic absorption in uniaxially strained germanium, *Phys. Rev. B* **97**, 155127 (2018).
- [22] K. Guilloy *et al.*, Germanium under high tensile Stress: Non-linear dependence of direct band gap vs strain, *ACS Photon.* **3**, 1907 (2016).
- [23] T. D. Eales *et al.*, $\text{Ge}_{1-x}\text{Sn}_x$ alloys: consequences of band mixing effects for the evolution of the band gap Γ -character with Sn concentration, *Sci. Rep.* **9**, 14077 (2019).
- [24] Y. M. Niquet, D. Rideau, C. Tavernier, H. Jaouen, and X. Blase, Onsite matrix elements of the tight-binding Hamiltonian of a strained crystal: application to silicon, germanium, and their alloys, *Phys. Rev. B* **79**, 245201 (2009).
- [25] Y.-M. Niquet and C. Delerue, Carrier mobility in strained Ge nanowires, *J. Appl. Phys.* **112**, 084301 (2012).
- [26] M. Virgilio, C. L. Manganelli, G. Grosso, G. Pizzi, and G. Capellini, Radiative recombination and optical gain spectra in biaxially strained *n*-type germanium, *Phys. Rev. B* **87**, 235313 (2013).
- [27] D. Rainko *et al.*, Impact of tensile strain on low Sn content GeSn lasing, *Sci. Rep.* **9**, 259 (2019).
- [28] N. W. Hendrickx, D. P. Franke, A. Sammak, G. Scappucci, and M. Veldhorst, Fast two-qubit logic with holes in germanium, *Nature (London)* **577**, 487 (2020).
- [29] G. Scappucci, C. Kloeffel, F. A. Zwanenburg *et al.*, The germanium quantum information route, *Nat. Rev. Mater.* **6**, 926 (2021).
- [30] D. Jirovec, A. Hofmann, A. Ballabio *et al.*, A singlet-triplet hole spin qubit in planar Ge, *Nat. Mater.* **20**, 1106 (2021).
- [31] J. Liu *et al.*, Tensile-strained, *n*-type Ge as a gain medium for monolithic laser integration on Si, *Opt. Express* **15**, 11272 (2007).
- [32] J. Liu, X. Sun, R. Camacho-Aguilera, L. C. Kimerling, and J. Michel, Ge-on-Si laser operating at room temperature, *Opt. Lett.* **35**, 679 (2010).
- [33] R. E. Camacho-Aguilera *et al.*, An electrically pumped germanium laser, *Opt. Express* **20**, 11316 (2012).
- [34] R. Koerner *et al.*, Electrically pumped lasing from Ge fabry-perot resonators on Si, *Opt. Express* **23**, 14815 (2015).
- [35] L. Carroll, P. Friedli, S. Neuenschwander, H. Sigg, S. Cecchi, F. Isa, D. Chrastina, G. Isella, Y. Fedoryshyn, and J. Faist, Direct-Gap Gain and Optical Absorption in Germanium Correlated to the Density of Photoexcited Carriers, Doping, and Strain, *Phys. Rev. Lett.* **109**, 057402 (2012).

- [36] S. A. Srinivasan *et al.*, Extraction of carrier lifetime in Ge waveguides using pump probe spectroscopy, *Appl. Phys. Lett.* **108**, 211101 (2016).
- [37] R. A. Minamisawa *et al.*, Top-down fabricated silicon nanowires under tensile elastic strain up to 4.5%, *Nat. Commun.* **3**, 1096 (2012).
- [38] M. J. Süess *et al.*, Analysis of enhanced light emission from highly strained germanium microbridges, *Nat. Photon.* **7**, 466 (2013).
- [39] J. Petykiewicz *et al.*, Direct bandgap light emission from strained germanium nanowires coupled with High-Q nanophotonic cavities, *Nano Lett.* **16**, 2168 (2016).
- [40] A. L. Schawlow and C. H. Townes, Infrared and optical masers, *Phys. Rev.* **112**, 1940 (1958).
- [41] T. Zabel *et al.*, Top-down method to introduce ultra-high elastic strain, *J. Mater. Res.* **32**, 726 (2017).
- [42] S. Tardif, Lattice strain and tilt mapping in stressed Ge microstructures using X-Ray laue micro-diffraction and rainbow filtering, *J. Appl. Cryst.* **49**, 1402 (2016).
- [43] R. Geiger *et al.*, Excess carrier lifetimes in Ge layers on Si, *Appl. Phys. Lett.* **104**, 062106 (2014).
- [44] J. B. Arthur, A. C. Baynham, W. Fawcett, and E. G. S Paige, Optical absorption due to free holes in Germanium: A comparison of theory and experiment, *Phys. Rev.* **152**, 740 (1966).
- [45] B. Daino, P. Spano, M. Tamburrini, and S. Piazzolla, Phase noise and spectral line shape in semiconductor lasers, *IEEE J. Quantum Electron.* **19**, 266 (1983).
- [46] P. M. Pearce, C. A. Broderick, M. P. Nielsen, and A. D. Johnson, Electronic and optical properties of $\text{Si}_x\text{Ge}_{1-x-y}\text{Sn}_y$ alloys lattice-matched to Ge, *Phys. Rev. Mater.* **6**, 015402 (2022).
- [47] R. Geiger *et al.*, Uniaxially stressed germanium with fundamental direct band gap, [arXiv:1603.03454](https://arxiv.org/abs/1603.03454).
- [48] F. Stern, Effect of band tails on stimulated emission of light in semiconductors, *Phys. Rev.* **148**, 186 (1966).
- [49] C. H. Henry, Theory of the linewidth of semiconductor lasers, *IEEE J. Quantum Electron.* **18**, 259 (1982).
- [50] T. P. Lee, C. A. Burrus, K. Y. Liou, N. A. Olsson, R. A. Logan, and D. P. Wilt, Measured spectral linewidth of single-frequency 1.3 and 1.5 μm injection lasers, *Electron. Lett.* **20**, 1011 (1984).
- [51] K. Kikuchi, T. Okoshi, and R. Arata, Measurement of linewidth and FM-noise spectrum of 1.52 μm InGaAsP lasers, *Electron. Lett.* **20**, 535 (1984).
- [52] K. Y. Liou, N. K. Dutta, and C. A. Burrus, Linewidth-narrowed distributed feedback injection lasers with long cavity length and detuned Bragg wavelength, *Appl. Phys. Lett.* **50**, 489 (1987).
- [53] D. Welford and A. Mooradian, Observation of linewidth broadening in (GaAl)As diode lasers due to electron number fluctuations, *Appl. Phys. Lett.* **40**, 560 (1982).
- [54] W. Elsässer, E. O. Göbel, and J. Kuhl, Coherence properties of gain- and index-guided semiconductor lasers, *IEEE J. Quantum Electron.* **19**, 981 (1983).
- [55] J. Harrison and A. Mooradian, Spectral characteristics of (GaAl)As diode lasers at 1.7 K, *Appl. Phys. Lett.* **45**, 318 (1984).
- [56] W. Elsässer and E. O. Göbel, Spectral linewidth of gain- and index-guided InGaAsP semiconductor lasers, *Appl. Phys. Lett.* **45**, 353 (1984).
- [57] K. Kojima, S. Noda, S. Tai, K. Kyuma, and T. Nakayama, Measurement of spectral linewidth of AlGaAs/GaAs distributed feedback lasers, *Electron. Lett.* **22**, 425 (1986).
- [58] D. W. Rush, G. L. Burdge, and P. T. Ho, The linewidth of a mode-locked semiconductor laser caused by spontaneous emission: Experimental comparison to single-mode operation, *IEEE J. Quantum Electron.* **22**, 2088 (1986).
- [59] K. Kobayashi and I. Mito, Progress in narrow-linewidth tunable laser sources, in *Proceedings of the OFC/IIOC* (1987), Vol. 1100, p. 14831.
- [60] M. J. O'Mahony and I. D. Henning, Semiconductor laser linewidth broadening due to $1/f$ carrier noise, *Electron. Lett.* **19**, 1000 (1983).
- [61] K. Kikuchi and T. Okoshi, Dependence of semiconductor laser linewidth on measurement time: Evidence of predominance of $1/f$ noise, *Electron. Lett.* **21**, 1011 (1985).
- [62] K. Vahala and A. Yariv, Occupation fluctuation noise: A fundamental source of linewidth broadening in semiconductor lasers, *Appl. Phys. Lett.* **43**, 140 (1983).
- [63] M. C. Amann and R. Schimpe, Excess linewidth broadening in wavelength-tunable laser diodes, *Electron. Lett.* **26**, 279 (1990).
- [64] M. C. Amann, The effect of spatial correlation on the linewidth broadening in tunable laser diodes, *IEEE J. Quantum Electron.* **29**, 1799 (1993).
- [65] C. Bonzon, Phase and mode control of structured semiconductor lasers, thesis ETH No. 23410 (2016).
- [66] E. M. T. Fadaly *et al.*, Direct-bandgap emission from hexagonal Ge and SiGe alloys, *Nature (London)* **580**, 205 (2020).
- [67] M. Grydlik *et al.*, Lasing from glassy Ge quantum dots in crystalline Si, *ACS Photon.* **3**, 298 (2016).
- [68] C. G. Van de Walle, Band lineups and deformation potentials in the model-solid theory, *Phys. Rev. B* **39**, 1871 (1989).
- [69] F. K. Reinhart, Direct determination of the free-carrier injection density, the free-carrier absorption, and the recombination factors in double heterostructure diodes by optical phase measurements. Part III, *J. Appl. Phys.* **97**, 123536 (2005).
- [70] P. Y. Yu and M. Cardona, *Fundamentals of Semiconductor—Physics and Materials Properties* (Springer-Verlag, Berlin, 2010).
- [71] H. Y. Fan, W. Spitzer, and R. J. Collins, Infrared absorption in n-type germanium, *Phys. Rev.* **101**, 566 (1956).
- [72] W. Elsässer and E. O. Göbel, Multimode effects in the spectral linewidth of semiconductor lasers, *IEEE J. Quantum Electron.* **21**, 687 (1985).